Materials Advances

ROYAL SOCIETY OF CHEMISTRY

PAPER

View Article Online
View Journal | View Issue

Cite this: *Mater. Adv.*, 2025, 6, 5959

A DFT study to evaluate the modulation in the band gap, elastic, and optical performances of $RbCdF_3$ under the influence of stress

M. Sana Ullah Sahar,[a] S. M. Junaid Zaidi,[b] Hammad Khalid[c] and M. Ijaz Khan *[c]

The effects of stress on the structural, mechanical, and optical properties of cubic rubidium cadmium fluoride ($RbCdF_3$) have been examined using computational methods based on density functional theory (DFT). Different levels of stress (0, 30, 60, and 86 GPa) were applied to analyze how these conditions influence the material's characteristics. Significant reductions in lattice parameters were observed, with the values decreasing from 4.5340 Å to 3.8516 Å, and the volume decreased by approximately 39%. An increase in the band gap of about 12% was noted, rising from 3.128 eV to 3.533 eV. Notable changes in optical properties, including reflectivity and absorption, were also recorded under stress, highlighting the material's potential for use in optoelectronic applications. The mechanical analysis revealed that $RbCdF_3$ exhibits both brittle and ductile behavior, suggesting a complex response to applied stress. The Pugh ratio indicated a degree of ductility, while the Cauchy pressure suggested a tendency toward ductile behavior. These findings imply that $RbCdF_3$ maintains structural stability under varying stress levels, providing valuable insights into how stress affects its properties. This understanding could inform future applications in electronic and optoelectronic devices, particularly in environments where stress may be a significant factor.

Received 29th April 2025,
Accepted 6th July 2025

DOI: 10.1039/d5ma00413f

rsc.li/materials-advances

1. Introduction

Cubic perovskites have recently emerged as highly efficient materials for converting solar energy into usable power, capturing the interest of researchers and industries alike.[1–3] Their unique properties, such as ionic conductivity, superconductivity,[4] large magnetoresistance, and wide range of dielectric values,[5–7] make perovskite-structured compounds particularly appealing for applications in microelectronics and telecommunications. The general formula for perovskites is ABX_3, where "X" represents an anion (either oxygen or a halogen), while "A" and "B" denote cations.[8] Recent years have seen a surge in interest surrounding these compounds, primarily due to their remarkable physicochemical characteristics.[9] Notably, when fluorine occupies the X position in ABF_3-type compounds, they are classified as fluoro perovskite compounds.[10] The arrangement of atoms in these structures is distinctive: "A" atoms are positioned at the corners (0, 0, 0), "F" atoms occupy the face-centered positions (FCC) at (0.5, 0, 0.5), and B atoms are located at the body-centered (BCC) coordinates (0.5, 0.5, 0.5).[11–14] The special properties of ternary fluorides (ABF_3), including their optical performance,[15,16] elevated temperature superionic conductivity,[17] semi-conductivity, ferroelectricity,[18] and antiferromagnetism,[19] hold promise for various technological applications.

Previous studies have investigated the optical and thermal properties of fluoro perovskites, as well as their potential applications in clinical diagnostics.[20,21] These materials stand out among inorganic compounds due to several key characteristics, including a relatively large band gap energy, low hygroscopicity, superior thermal and mechanical stability,[22] and exceptional clarity extending into the near-infrared range.[23] These attributes make them valuable candidates for use as lenses in laser lithography.[24] Furthermore, fluoro perovskite materials have been reported to have applications in radiotherapy dosimetry.[25,26] Fekhra *et al.*[27] compared the structural, electrical, elastic, and optical properties of halide perovskites $SiAuF_3$ and $SiCuF_3$ using density functional theory (DFT). They found that $SiAuF_3$ exhibited improved reflectivity at low energies, while $SiCuF_3$ demonstrated a better refractive index and enhanced mechanical stability. Both materials displayed strong absorption characteristics, indicating their potential for optoelectronic applications.

[a] *Department of Mechanical, Industrial, and Energy Systems, University of Sargodha, Sargodha 40100, Pakistan. E-mail: ijazkhan4123@gmail.com*
[b] *Department of Physics and Mathematics, Faculty of Sciences, Superior University, Lahore 54000, Pakistan*
[c] *Institute of Mechanical and Manufacturing Engineering, Khwaja Fareed UEIT, Rahim Yar Khan, 64200, Pakistan*

Among the fluoro perovskite group, rubidium lead fluoride ($RbPbF_3$) stands out due to its cubic crystal structure and potential applications in the lithography industry. It is classified under the space group $Pm\bar{3}m$.[28] While experimental research on RPF has yielded promising results, the theoretical understanding of its optical and electronic properties remains limited. Notably, temperature-dependent morphological phase changes have been observed experimentally.[29] Several researchers have utilized the generalized gradient approximation (GGA) technique to investigate the electronic bandgap of RPF. For example, Fakiha *et al.*[30] simulated RPF using GGA, identifying semiconducting behavior for both doped and undoped variants, as well as variations in lattice constants. They also noted an increase in loss function and refractive index, alongside changes in elastic and mechanical properties. Similarly, Iqra *et al.*[31] performed calculations using GGA–PBE with the CASTEP code, analyzing the effects of pressure and reporting a lattice constant of 4.59 Å, a bulk modulus of 63.7821, and an energy bandgap of 2.863 eV at 0 GPa, alongside a decrease in refractive index from 2.6 to 1.72 under pressure.

Further investigations by Murtaza *et al.*[32] revealed a lattice constant of a = 4.459 Å, a bulk modulus of B = 62.37 GPa, and elastic constants C_{11} = 122.46, C_{12} = 32.32, and C_{44} = 19.90. By applying the Becke Johnson potential (TB-mBJ), they addressed the electronic properties of RPF. Abderrahmane *et al.*[33] also applied the GGA–PBE approximation, finding a lattice parameter of a = 4.500 Å and a bulk modulus of B = 53.36 GPa, with the band gap calculated using the WC-GGA method. Their calculated values were in good agreement with experimental data.[34] Additionally, the electronic, mechanical, and thermoelectric properties of alkaline perovskites $ACdF_3$ (where A = K, Rb, Cs) were examined using the FP-LAPW technique from the perspective of DFT, revealing an indirect bandgap and an increase in bulk modulus with pressure. Despite the existing literature on pure RPF, there remains a significant gap regarding the effects of applied stress on its properties. This study aims to address this gap by comparing stressed and unstressed compounds to observe how various properties, including electronic, structural, optical, elastic, mechanical, and thermodynamic characteristics, are affected. Utilizing density functional theory (DFT), we have investigated the density of states (DOS), absorption, dielectric constant, reflectivity, energy loss function, refractive index, and more, through the generalized gradient approximation and Perdew–Burke–Ernzerhof (GGA–PBE) exchange–correlation method. To discern the distinctions in RPF, we examined the influence of stress (ranging from 0 to 86 GPa) using the CASTEP code. This research has explored the deviations in lattice parameters, physical stability, and anisotropic properties of pure compounds under the influence of stress.

The primary objective of this study is to investigate the influence of applied stress on the structural, electronic, optical, and mechanical properties of cubic rubidium cadmium fluoride ($RbCdF_3$) using density functional theory (DFT). Specifically, the research assesses the modulation of the band gap, elastic properties, and optical performance of $RbCdF_3$ under varying stress conditions (0, 30, 60, and 86 GPa). A critical aspect is to determine whether the material retains its cubic structure and stability as stress increases, and to analyse the implications for potential applications. While previous studies may have examined individual properties of $RbCdF_3$ or related materials, this work provides a comprehensive analysis across multiple property domains under systematically varied stress. Notably, the findings reveal a dual mechanical response, exhibiting both brittle and ductile characteristics, which offers new insights into the material's suitability for various applications. This multifaceted approach enhances the understanding of $RbCdF_3$ and establishes a foundation for future research into analogous materials, thereby distinguishing this study within the field.

2. Computational details

The Material Studio suite was used in this study to calculate the structural, electronic, optical, and mechanical properties of $RbCdF_3$. The plane wave pseudopotential approach, grounded in density functional theory (DFT) principles,[35–38] was implemented using the Cambridge Serial Total Energy Package (CASTEP) code. The generalised gradient approximation formulated by Perdew, Burke, and Ernzerhof (GGA–PBE) was adopted to approximate the exchange–correlation energy of the many-electron system.[39,40] As illustrated in Fig. 1(a), the computational model applies the GGA method to a cubic $RbCdF_3$ structure with space group $Pm\bar{3}m$, subjected to external stress values of 0, 30, 60, and 86 GPa, using a $1 \times 1 \times 1$ unit cell. Plane wave basis sets were employed, with an $8 \times 8 \times 8$ Monkhorst–Pack grid used for Brillouin zone integration. Electron–ion interactions were described using ultrasoft pseudopotentials, with a cutoff energy of 260 eV. The convergence criterion for total energy was set at 1×10^{-5} eV. Fig. 1(b) demonstrates the variation in lattice parameters and unit cell volume under increasing stress. The results indicate that both parameters decrease as external stress rises, with the lattice parameter decreasing from 4.5340 Å to 3.8516 Å up to 86 GPa. The Kohn–Sham equations[41] were employed to solve the electronic structure. Fig. 1(c) shows the effect of stress on the band gap. Notably, the calculated band gap and lattice parameter values are in excellent agreement with previous studies, as presented in Table 1.

3. Electronic properties

The complete symmetrical bars of the Brillouin zone at 0 GPa were used to analyse the electronic band structure of cubic $RbCdF_3$, as shown in Fig. 2(a)–(d). The electronic and optical properties were investigated based on the crystallographic parameters of $RbCdF_3$. Band gap calculations were conducted using the exchange–correlation functional within the PBE framework. In general, two types of band gaps are observed: direct and indirect. A direct band gap occurs when the valence band maximum and conduction band minimum are located at

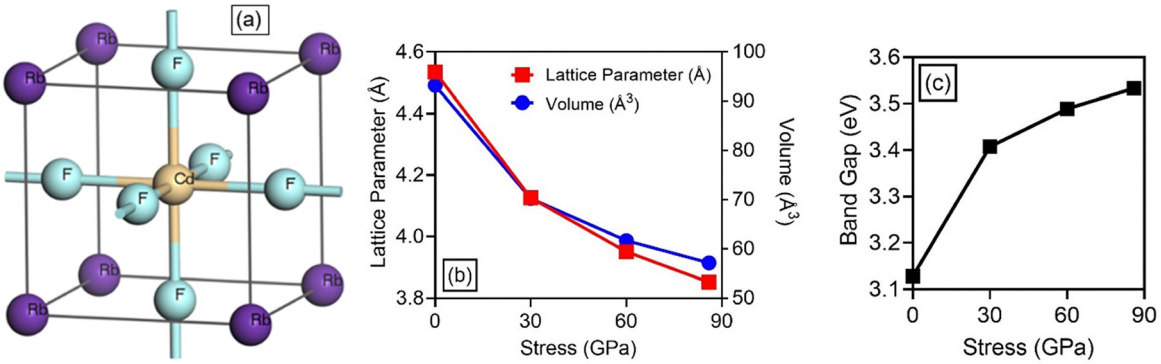

Fig. 1 (a) $RbCdF_3$ unit cell, (b) lattice parameters "*a*" and cell volume "*V*" plotted with stress, and (c) bandgap *vs.* stress.

Table 1 Lattice parameters and bandgap comparison

$RbCdF_3$ at 0 GPa	Lattice parameter (Å)	Band gap (eV)
Present work	4.5340	3.128
Theoretical	4.59,[31] 4.459,[32] 4.500,[33] 4.503[34]	2.863,[31] 3.07,[33] 3.223[34]
Experimental	Ref. 42, 4.399[43]	

the same *k*-point, whereas an indirect band gap arises when they occur at different *k*-points. For $RbCdF_3$ at 0 GPa, the calculated energy band gap is 3.128 eV. As the applied stress increases, the band gap widens, reaching approximately 3.533 eV at 86 GPa, representing an increase of about 12%, as depicted in Fig. 1(c). This trend suggests a near-linear relationship between applied stress and band gap expansion, with the cubic structure remaining stable up to 86 GPa. The observed increase in the band gap under stress is likely due to complex interactions, such as reduced orbital overlap and variations in bond length. A detailed examination of the density of states and charge density distributions would provide further insights into the mechanisms responsible for this behaviour. Including such analyses in the manuscript would enrich its scientific depth and offer a more comprehensive interpretation of the results.

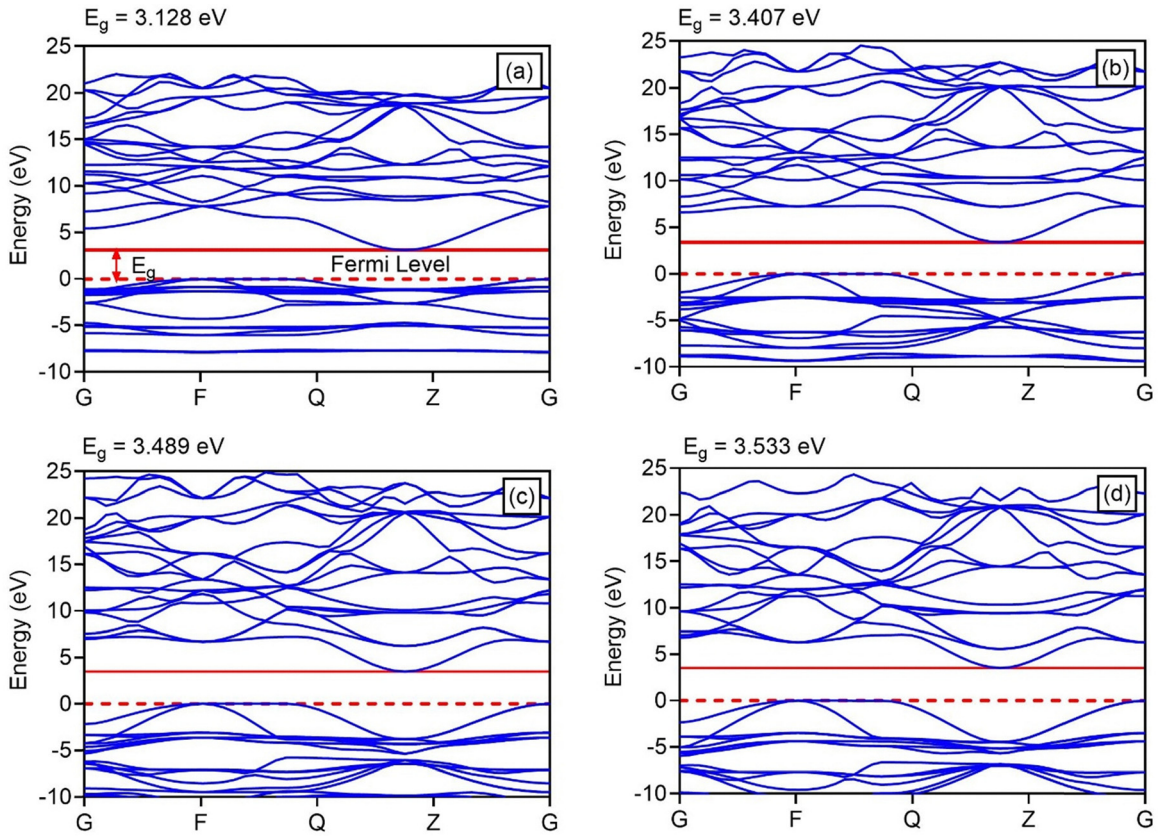

Fig. 2 Band structure of $RbCdF_3$ at (a) 0 GPa, (b) 30 GPa, (c) 60 GPa, and (d) 86 GPa.

4. Optical properties

The optical properties of $RbCdF_3$, including its absorption coefficient, real and imaginary parts of the optical conductivity, real and imaginary components of the dielectric function, energy loss function, reflectivity, and real and imaginary refractive indices, were evaluated to explore the interaction between light and the material. Eqn (1)–(8) were used to estimate optical properties.[44,45] Fig. 3(a)–(f) illustrates the measurement of various optical properties at 0, 30, 60, and 86 GPa.

$$I(\omega) = \sqrt{2}\omega\left(\sqrt{\varepsilon_1(\omega)^2+\varepsilon_2(\omega)^2} - \varepsilon_1(\omega)\right)^{1/2} \quad (1)$$

$$K(\omega) = \frac{I(\omega)}{2\omega} \quad (2)$$

$$L(\omega) = \frac{\varepsilon}{\left(\varepsilon_1(\omega)^2+\varepsilon_2(\omega)^2\right)} \quad (3)$$

$$n(\omega) = \left(\frac{1}{\sqrt{2}}\right)\left(\sqrt{\varepsilon_1(\omega)^2+\varepsilon_2(\omega)^2} - \varepsilon_1(\omega)\right)^{1/2} \quad (4)$$

$$r(\omega) = \frac{n+iK-1}{n+iK+1} \quad (5)$$

$$\sqrt{\varepsilon(\omega)} = n(\omega) + iK(\omega) \quad (6)$$

$$\varepsilon_1(\omega) = n^2 - K^2 \quad (7)$$

$$\varepsilon_2(\omega) = 2nK \quad (8)$$

where $n(\omega)$, $r(\omega)$, $K(\omega)$, $L(\omega)$, and $\varepsilon(\omega)$, $\varepsilon_1(\omega)$ and $\varepsilon_2(\omega)$ are the reflective index, the reflectivity coefficient, the degree of

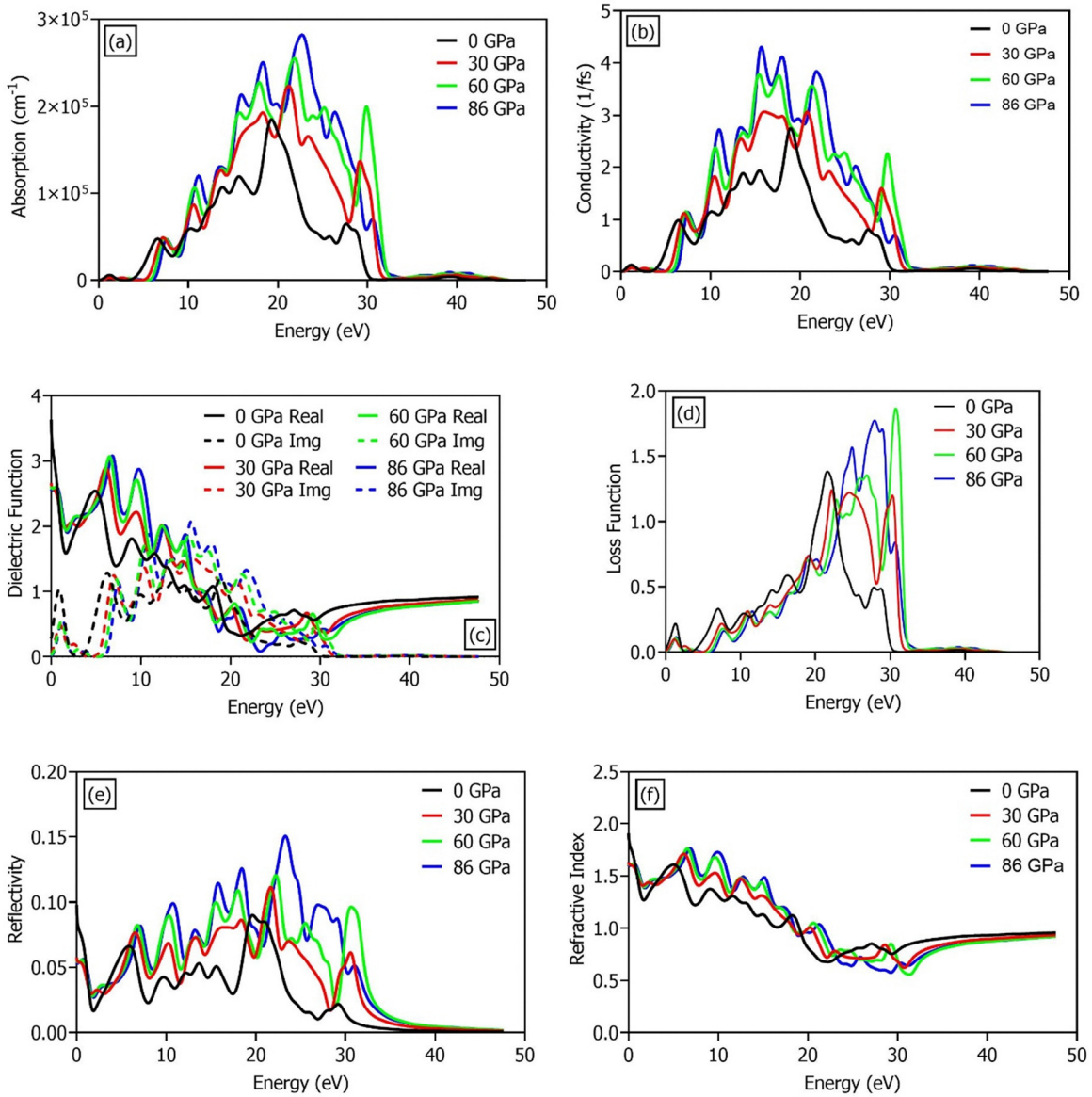

Fig. 3 Optical properties of $RbCdF_3$ (a) absorption, (b) conductivity, (c) dielectric function, (d) loss function, (e) reflectivity, and (f) refractive index.

extinction factor, the amount of energy loss function, the function of the dielectric, and the real part, and the imaginary part of the dielectric.

Fig. 3(a) presents the absorption spectra of $RbCdF_3$ under various applied stress levels. The material exhibits substantial absorption in the ultraviolet region. The threshold energy, which denotes the minimum photon energy that the material can effectively absorb, increases with applied stress, resulting in a shift of the absorption edge towards higher energies. At 0 GPa, the absorption edge is approximately 5 eV. Such features in the optical spectra may indicate higher-order interband transitions or contributions from excitonic effects, which are not fully accounted for in conventional DFT calculations. As the applied stress increases from 0 to 86 GPa, the absorption peaks become sharper and shift towards higher energies, demonstrating a clear blue shift. Notably, at 86 GPa, the spectrum exhibits its maximum absorption peak at around 23 eV. The position of the absorption edge correlates with the band gap energy, as the absorption onset occurs at wavelengths corresponding to the band gap. According to Fig. 2(c), the calculated band gap of $RbCdF_3$ is indirect, which typically results in a less pronounced or more gradual absorption edge, as evident in Fig. 3(a). Although the fundamental band gap is approximately 3.128 eV at 0 GPa, the absorption spectra indicate significant absorption of photons with energies up to about 19–23 eV, likely due to higher-order transitions.

Fig. 3(b) illustrates the variation in optical conductivity of $RbCdF_3$ under applied stresses ranging from 0 to 86 GPa. The results indicate that conductivity increases with stress, with the highest intensity peaks shifting towards higher energies, consistent with the observed band gap widening. Fig. 3(c) presents the real and imaginary parts of the dielectric function as functions of photon energy for stress levels of 0, 30, 60, and 86 GPa. The static dielectric constant decreases from approximately 3.6 at 0 GPa to around 2.5 at 86 GPa. This reduction can be attributed to changes in both the polarizability and ion displacement within the crystal lattice. Applied stress compresses the lattice, altering the electronic environment and the spatial configuration of ions, which diminishes the material's ability to polarise in response to an external electric field. The real part of the dielectric function describes the material's capacity for polarisation, while the imaginary part accounts for energy dissipation due to absorption. The computed results confirm that these features are related to electronic transitions from the valence band to the conduction band, in line with the electronic structure discussed earlier.

A moderate dielectric constant and an intermediate energy band gap were observed for $RbCdF_3$ through simulation. Materials exhibiting such balanced properties are widely utilised across various technologies, including electronic devices, solar cells, sensors, and other components that demand an optimal combination of electronic characteristics, thermal stability, and optical performance. The characteristic plasmonic oscillations are described by the electron energy loss function, $L(\omega)$, which is presented in Fig. 3(d). The energy loss function characterises both the macroscopic and microscopic interactions as fast electrons traverse the material, initiating the energy loss process. The most prominent peak in the energy loss spectrum corresponds to the plasmon resonance. The energies of the major plasmon peaks were determined to be approximately 21.6 eV at 0 GPa, 23.4 eV at 30 GPa, 33.7 eV at 60 GPa, and 30.6 eV at 86 GPa, indicating a clear shift with increasing stress and providing estimates of the volume plasmon energy.

Fig. 3(e) illustrates the reflectivity as a function of photon energy under varying stress conditions. At 0 GPa, a significant reflectivity peak is observed in the ultraviolet region at approximately 19.6 eV, with overall reflectivity remaining relatively low at lower photon energies, indicating high transparency in the visible and lower UV range. In contrast, at elevated stress levels (30, 60, and 86 GPa), reflectivity is comparatively higher within the 2–19 eV range. These findings suggest that $RbCdF_3$ exhibits considerable potential for applications in ultraviolet shielding and optoelectronic devices, owing to its high UV reflectivity and transparency in other regions. Fig. 3(f) displays the refractive index as a function of photon energy for stresses ranging from 0 to 86 GPa. The static refractive index at zero photon energy reflects the material's inherent transparency and its capacity to interact with light. The results clearly show that the refractive index decreases with increasing photon energy across all stress conditions, demonstrating dispersive behaviour typical of dielectric materials. The moderate refractive index values observed for $RbCdF_3$ suggest potential for various optical applications where precise control of light transmission, reduced reflectivity, and tailored optical effects are desirable, further highlighting the material's practical significance.

5. Elastic and mechanical behavior

Elastic constants play a crucial role in characterizing the mechanical properties of a material, including its stability, stiffness, and hardness.[30] For a cubic crystal structure, as illustrated in Fig. 4, the elastic behaviour is described by three independent elastic constants: C_{11}, C_{12}, and C_{44}.[46] The coefficient C_{11} primarily relates to longitudinal and shear stresses along the principal axes, while C_{12} accounts for the material's transverse response to stress. The cubic structure of $RbCdF_3$ satisfies the Born stability criteria,[36] ensuring mechanical

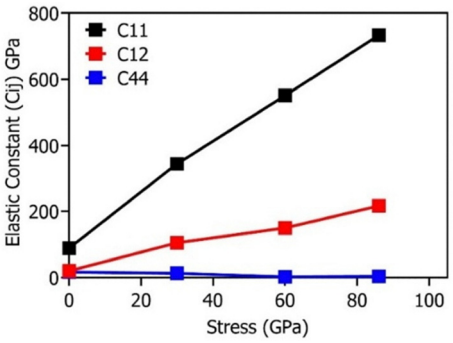

Fig. 4 Elastic constants plotted as a function of stress.

stability under applied stress. The specific conditions for the elastic stability of a cubic system are given by:

$$(C_{11} - C_{12}) > 0, \quad C_{11} > 0, \quad C_{44} > 0, \quad C_{12} < B < C_{11}, \quad (C_{11} + 2C_{12}) > 0. \tag{9}$$

An essential parameter for evaluating a material's rigidity is its Young's modulus. The elastic constants C_{11}, C_{12}, and C_{44} were determined and subsequently used to calculate the relevant mechanical properties.[47] Young's modulus (E) and Poisson's ratio (ν) were estimated using eqn (10) and (11). The bulk modulus (B) and shear modulus (G) were derived from the Reuss and Voigt bounds for shear (G_R) and (G_V) and bulk (B_R and B_V) moduli, as shown in eqn (12)–(14).

$$E = \frac{9GB}{3B + G} \tag{10}$$

$$\nu = \frac{3B - G}{2(3B + G)}. \tag{11}$$

$$G_V = \frac{1}{5}(3C_{44} + C_{11} - C_{12}) \tag{12}$$

$$G_R = \frac{5(C_{11} - C_{12})C_{44}}{3(C_{11} - C_{12}) + 4C_{44}} \tag{13}$$

$$B_V = B_R = \frac{C_{11} + 2C_{12}}{3}. \tag{14}$$

The bulk modulus (B) is a key parameter for characterizing the stiffness and incompressibility of a material. A higher value of B indicates greater resistance to uniform compression, reflecting increased rigidity and structural tightness. In the present study, the computed results show that the maximum bulk modulus reaches 388.78 GPa at an applied stress of 86 GPa, as illustrated in Fig. 5(a). This trend demonstrates that the stiffness of the material progressively increases with rising stress levels from 0 to 86 GPa.

Higher values of bulk modulus (B) and shear modulus (G) indicate a compound's greater resistance to deformation, reflecting its intrinsic stiffness and mechanical stability. Similarly, Young's modulus (E) is a key indicator of stiffness, with its value increasing alongside applied stress, as demonstrated in Fig. 5(a). According to the results summarised in Table 2, Young's modulus rises from 57.72 GPa to 161.81 GPa as the stress increases from 0 to 86 GPa, further evidencing the compound's enhanced rigidity under stress. The Pugh ratio (B/G) was employed to assess the material's ductility or brittleness. Following Pugh's criterion, a material is considered brittle if $B/G < 1.75$ and ductile if $B/G > 1.75$. In this study, the calculated B/G ratios for $RbCdF_3$ exceed 1.75 across the stress range, indicating a predominantly brittle nature, as depicted in Fig. 5(b). In addition, the G/B ratio provides complementary insight: values below 0.57 typically indicate ductility, while values above 0.57 imply brittleness, according to the Frantsevich rule. For $RbCdF_3$, the computed G/B ratios remain below 0.57 under all stress conditions, supporting the conclusion of a ductile tendency. Cauchy pressure (P_C), which was derived from elastic constants ($C_{12} - C_{44}$), further corroborates this interpretation; positive values signify ductility, whereas negative values suggest brittleness. The positive Cauchy pressure across the stress range of 0–86 GPa confirms the ductile behaviour of $RbCdF_3$, as shown in Fig. 5(c).

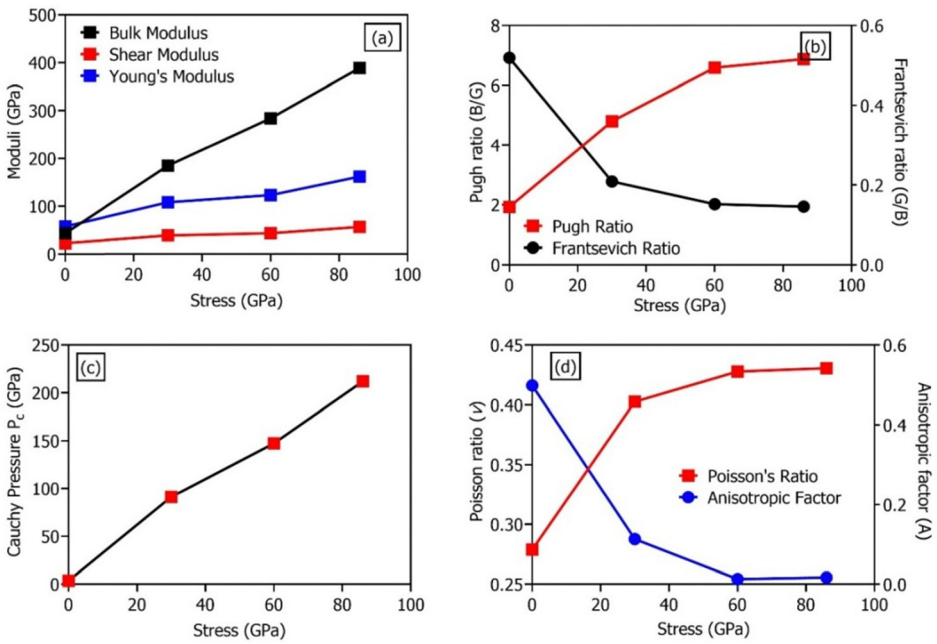

Fig. 5 Mechanical properties of $RbCdF_3$ *versus* applied stress (a) Bulk, Shear, and Young's moduli, (b) Pugh's ratio and Frantsevich ratio, (c) Cauchy pressure, (d) Poisson ratio and anisotropic factor.

Table 2 Comparison of the present calculations with theoretical and experimental data

Properties	Present calculations	Theoretical calculations	Experimental data
B (GPa)	43.5099	62.37,[a] 61.515,[b] 53.65[c]	
E (GPa)	57.7224	72.63,[a] 66.002[b]	
G (GPa)	22.5673	27.79,[a] 27.169[b]	
C_{11}	89.01205	122.46,[a] 117.2,[b] 162.75[c]	109.6[d]
C_{12}	20.7588	32.32,[a] 33.6,[b] 36.69[c]	37.3[d]
C_{44}	17.0093	19.90,[a] 17.4,[b] 24.09[c]	20.4[d]
ν	0.2789	0.305,[a] 0.321[b]	
B/G	1.928	2.24,[a] 2.461[b]	
A	0.4984	0.441,[a] 0.9732[b]	

[a] Ref. 32. [b] Ref. 33. [c] Ref. 34. [d] Ref. 48.

Poisson's ratio (ν) is another significant parameter for distinguishing ductile and brittle behaviour. For $RbCdF_3$, the Poisson's ratio remains greater than 0.26 throughout, reinforcing the material's elastic and ductile characteristics, as indicated in Fig. 5(d). Additionally, elastic anisotropy was evaluated using eqn (15). An anisotropy factor (A) equal to unity indicates isotropy, while deviations reflect anisotropy. As shown in Fig. 5(d), $RbCdF_3$ exhibits an anisotropy factor slightly below unity across the applied stress range, suggesting near-isotropic elastic behaviour.

$$A = \frac{2C_{44}}{C_{11} - C_{12}} \quad (15)$$

6. Thermodynamic characteristics

The thermodynamic properties of $RbCdF_3$, including entropy, heat capacity, Debye temperature, free energy, and enthalpy, were computed under applied stresses ranging from 0 to 86 GPa, as illustrated in Fig. 6(a)–(e). The trends indicate that the enthalpy, entropy, and heat capacity decrease with increasing stress when plotted as a function of temperature (0–1000 K). Conversely, the values of free energy and Debye temperature exhibit an increasing trend under applied stress; however, no significant variations were observed between 60 and 86 GPa, as shown in Fig. 6(a)–(e).

Fig. 7(a)–(d) depict the phonon dispersion curves for $RbCdF_3$ at 0 K under different applied stresses of 0, 30, 60, and 86 GPa. These results demonstrate that the phonon dispersion comprises numerous frequency modes, with a significant presence of imaginary modes, indicating the potential dynamical instability of the cubic structure at absolute zero. Similar observations at 0 GPa have been reported by Peijun Guo *et al.*,[49] corroborating the current findings. The application of stress can change interatomic distances and modify the effective force constants among atoms. Enhanced bond strength or increased force constants tend to produce higher-frequency phonon modes, thereby widening the energy gaps between distinct phonon branches or modes. Such stress-induced modifications in phonon gaps can significantly influence the material's thermal conductivity and mechanical properties, as evidenced by the variations in elastic, mechanical, and thermodynamic characteristics presented in Fig. 4–6. As shown in Fig. 7(a), a distinct phonon gap is apparent at 0 GPa, which broadens progressively with increasing applied stress up to 60 and 86 GPa. Furthermore, the expansion of the imaginary phonon modes across the stress range from 30 to 86 GPa, illustrated in Fig. 7(a)–(d), further indicates dynamical instability under these conditions. The persistence of imaginary frequencies implies that, despite the anisotropy factor suggesting near-isotropic behaviour, the cubic phase may not be structurally stable at 0 K. This apparent contrast underscores the complex behaviour of $RbCdF_3$ and highlights the necessity for further comprehensive investigations into its dynamical stability and potential phase transitions under varying thermodynamic and mechanical conditions.

7. Electron energy loss spectroscopy (EELS)

Essential elements of the electron energy loss spectroscopy (EELS) investigation include the energy-loss function and the identification of the principal peaks in the energy-loss spectrum, which enable investigation of the material's electronic structure and related properties.[50] Across the full stress range from 0 to 86 GPa, the emission and absorption spectra for Rb, Cd, and F atoms within the $RbCdF_3$ compound are presented in Fig. 8(a)–(f). For the Rb atom, the maximum absorption is observed at 14.64 eV, whereas the emission peak occurs at −7.58 eV. The electronic configuration of the Rb atom is $1s^2\ 2s^2\ 2p^6\ 3s^2\ 3p^6\ 4s^2\ 3d^{10}\ 4p^6\ 5s^1$, reflecting its partially filled valence shell, which contributes to these distinctive spectral features. These variations in the absorption and emission characteristics highlight the remarkable sensitivity of EELS analysis to subtle structural perturbations. Such shifts may arise from variations in lattice constants, changes in the local coordination environment, or alterations in interatomic distances under different stress conditions. Understanding these subtle modifications is critical for elucidating the material's electronic interactions and provides a valuable foundation for tailoring its properties for advanced functional applications.

For the Cd atom, the electronic configuration is $1s^2\ 2s^2\ 2p^6\ 3s^2\ 3p^6\ 4s^2\ 3d^{10}\ 4p^6\ 5s^2\ 4d^{10}$. At 0 GPa, the absorption peak for cadmium is observed at 14.32 eV, while the emission peak occurs at −1.90 eV. As illustrated in Fig. 8(b), the application of stress results in a discernible shift towards higher-energy absorption spectra, which can be attributed to variations in the density of states and alterations in the local electronic environment of the Cd atoms under compression. In the case of fluorine (F), which has the electronic configuration $1s^2\ 2s^2\ 2p^5$, a similar trend is evident. The maximum absorption for the fluorine atom occurs at approximately 10.39 V, as shown in Fig. 8(c) and (e). The energy-loss spectrum reveals notable shifts in response to applied stress, indicating that fluorine atoms experience electronic transitions that involve excitations from lower to higher energy levels. Moreover, the emission spectra exhibit comparable behaviour, highlighting the sensitivity of

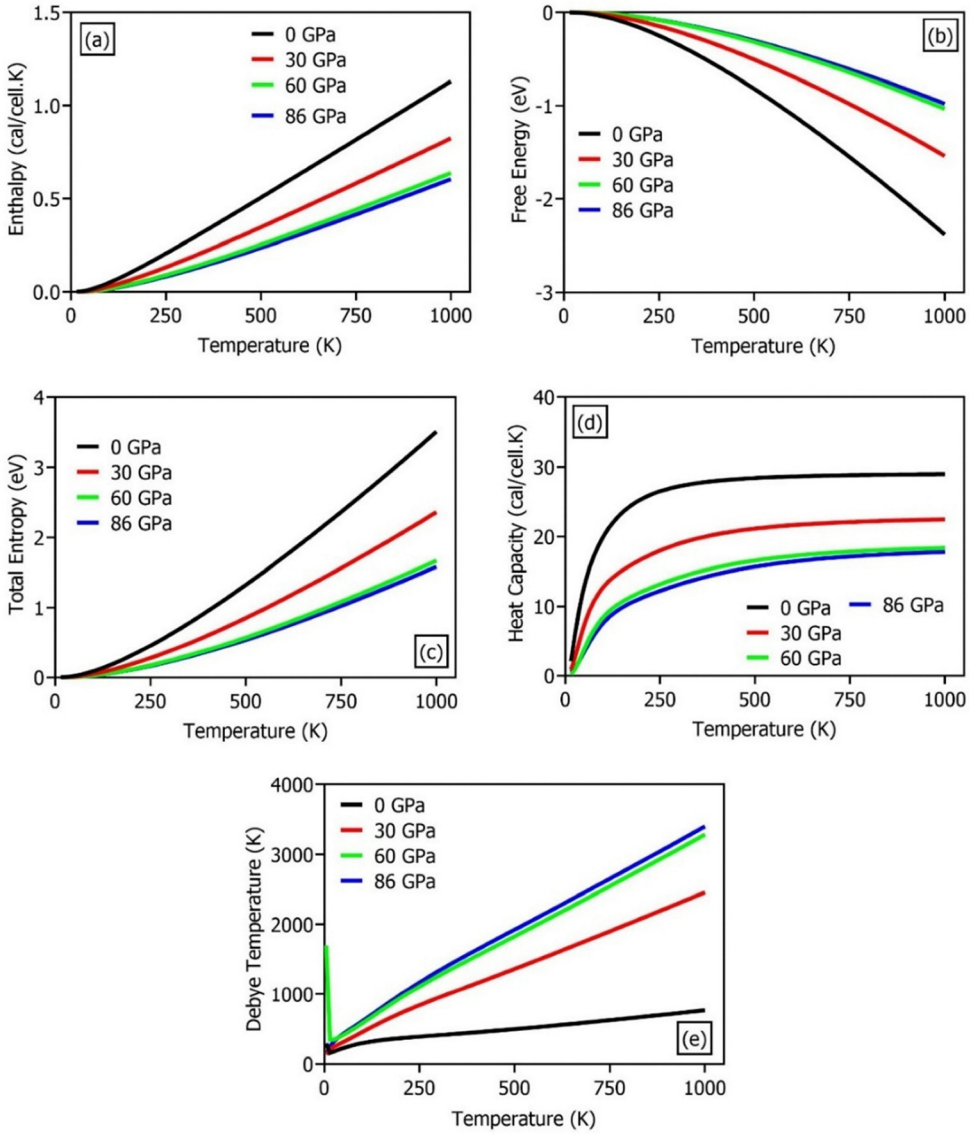

Fig. 6 Thermodynamic characteristics (a) enthalpy, (b) free energy, (c) total entropy, (d) heat capacity, and (e) Debye temperature for $RbCdF_3$.

the fluorine sites to external perturbations. These spectral variations, observed consistently across Rb, Cd, and F atoms, underscore the pronounced influence of stress-induced changes on the electronic structure of $RbCdF_3$. Such findings reinforce the importance of EELS as a diagnostic tool for probing subtle modifications in bonding, coordination, and electronic interactions within complex fluoroperovskite systems. Integrating these insights with the band structure, optical, and phonon analyses provides a comprehensive understanding of the material's response to external stress, thereby informing its potential application in advanced electronic and optoelectronic devices.

8. X-ray diffraction

Under stress conditions ranging from 0 to 86 GPa, the theoretical X-ray diffraction (XRD) analysis, presented in Fig. 9, provides valuable insights into the crystal structure and potential phase stability of the material under investigation. While direct experimental comparisons of theoretical XRD patterns for $RbCdF_3$ are limited in the existing literature, analogous studies support the preservation of its cubic structure under varying stress conditions, thereby corroborating the computational findings. The subtle shifts observed in the diffraction peaks with increasing stress suggest slight variations in the lattice parameters, reflecting the material's structural adaptability. Such dynamic adjustments highlight the compound's capacity to accommodate external pressures without undergoing significant phase transitions, a property that may be advantageous for applications requiring structural resilience and tunable performance.

Furthermore, these variations in diffraction patterns underscore the potential impact of stress on the electronic and mechanical properties of $RbCdF_3$, as lattice distortions can

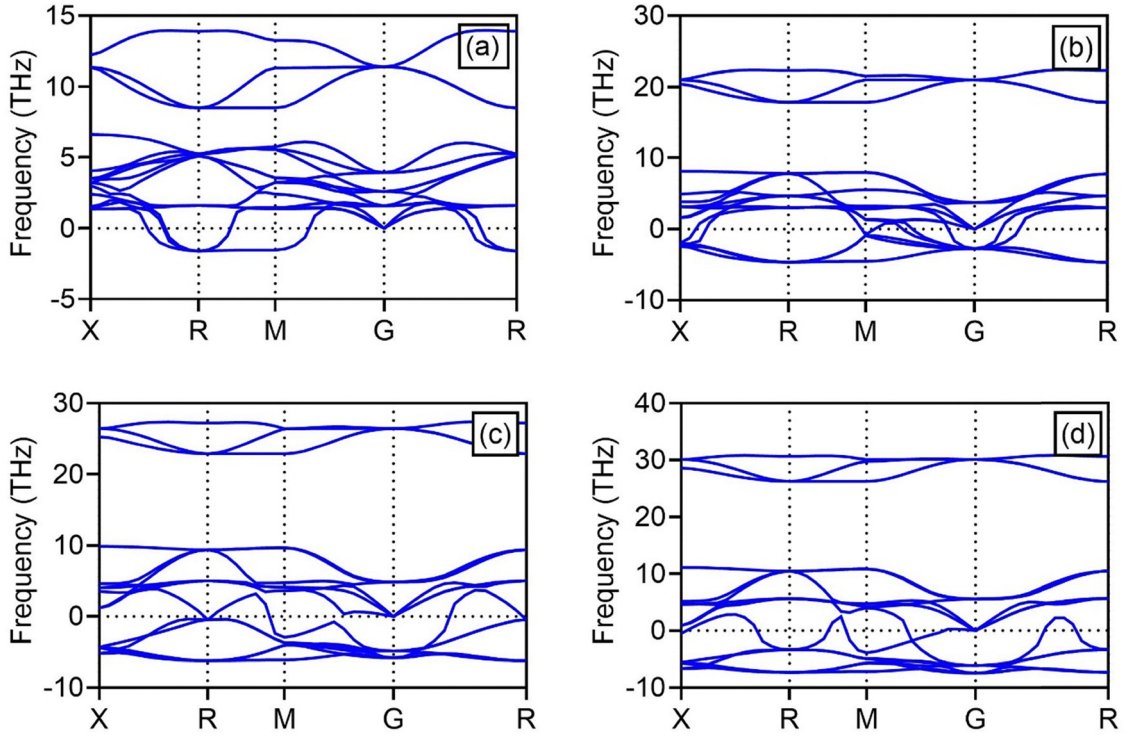

Fig. 7 Phonon dispersion of $RbCdF_3$ at (a) 0 GPa, (b) 30 GPa, (c) 60 GPa, and (d) 86 GPa.

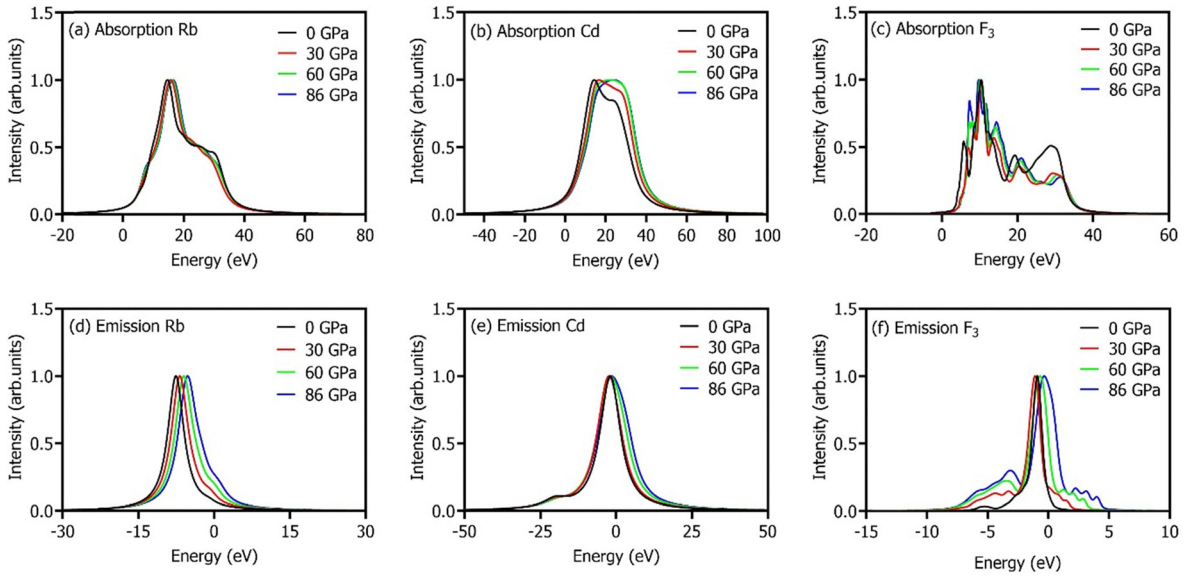

Fig. 8 EELS analysis, (a–c) absorption, and (d–f) emission of the constituent elements of $RbCdF_3$ at varying stress (0–86 GPa).

directly influence the band structure, carrier mobility, and elastic moduli. Of particular note is the phenomenon of destructive interference at larger scattering angles, which results in reduced intensity due to phase discrepancies arising from differences in path lengths of the scattered waves. As illustrated in Fig. 9(b), the intensity *versus* scattering vector plot demonstrates that at higher stress levels, specifically at 30 and 60 GPa, the diffraction peak intensities are noticeably greater than at 0 GPa. This increase in intensity implies enhanced constructive interference under these conditions, further confirming the material's structural coherence and the potential for controlled stress-induced modifications. Taken together, these theoretical XRD results reinforce the understanding of $RbCdF_3$ as a structurally stable and adaptable compound, with

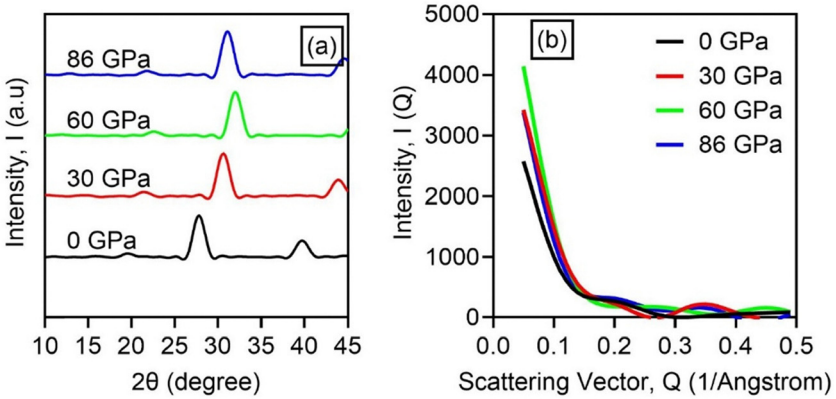

Fig. 9 X-ray diffraction analysis of $RbCdF_3$ (a) variation of X-ray intensity *versus* 2θ, and (b) variation of X-ray intensity *versus* scattering vector.

tunable characteristics that may be leveraged in advanced technological applications such as high-pressure optoelectronic devices and stress-responsive functional materials.

9. Conclusion

In this study, the electronic, optical, mechanical, thermodynamic, and structural properties of cubic $RbCdF_3$ were comprehensively investigated under various stress conditions ranging from 0 to 86 GPa, employing first-principles calculations within the PBE generalised gradient approximation framework. The optimized lattice parameters and cell volumes exhibited a systematic decrease with increasing stress, confirming the material's structural compressibility. The electronic band structure analyses revealed that the band gap of $RbCdF_3$ increased from 3.128 eV to 3.533 eV as stress was increased, suggesting tunable semiconducting behaviour suitable for optoelectronic applications. The optical characterization demonstrated enhanced conductivity, dielectric function, absorption coefficient, reflectivity, and refractive index with increasing stress, with the highest absorption reaching 28 2035.5 cm^{-1} at 86 GPa. Such promising optical responses imply potential utility in ultraviolet shielding, sensors, and high-performance optoelectronic devices. Mechanical stability was confirmed through the computed elastic constants, satisfying the Born stability criteria for a cubic phase. The moduli results indicated increased bulk, shear, and Young's moduli with rising stress, reflecting greater stiffness and reduced compressibility. The Pugh's ratio ($B/G > 1.75$), positive Cauchy pressure, Poisson's ratio exceeding 0.26, and Frantsevich ratio consistently supported the ductile nature of $RbCdF_3$ across all stress conditions. The material displayed slight elastic anisotropy, with the anisotropy factor (A) remaining below unity throughout, implying near-isotropic mechanical behaviour.

Furthermore, phonon dispersion analyses highlighted the presence of imaginary modes at 0 K, suggesting potential dynamical instabilities in the ideal cubic phase and underscoring the need for further finite-temperature or anharmonic investigations. Thermodynamic properties, including entropy, enthalpy, heat capacity, free energy, and Debye temperature, were systematically influenced by stress, providing additional insights into the compound's stability and performance under varying environmental conditions. Theoretical XRD patterns confirmed the retention of the cubic structure with minor lattice adjustments, reflecting the material's adaptability under applied stress. Overall, this study demonstrates that $RbCdF_3$ possesses a desirable combination of tunable electronic structure, favourable optical characteristics, ductile mechanical behaviour, and structural stability under high-stress conditions. These attributes collectively suggest that $RbCdF_3$ is a promising candidate for advanced optoelectronic, UV shielding, and high-pressure device applications. Future experimental validation and in-depth phonon analyses are recommended to further corroborate these findings and explore the material's performance under practical working environments.

Conflicts of interest

The authors have no conflicts of interest to declare.

Data availability

Research data will be made available upon reasonable request.

References

1 M. M. Al-Anazy, M. A. Ali and S. Bouzgarrou, *et al.*, Study of optoelectronic and thermoelectric properties of double perovskites for renewable energy, *Phys. Scr.*, 2021, **96**, 125828, DOI: 10.1088/1402-4896/AC297A.
2 H. Albalawi, S. A. Rouf and T. Zelai, *et al.*, The study optical, thermoelectric, and thermodynamic properties of double perovskites K_2CuBiX_6 (X = Cl, Br, I) for energy harvesting, *Mater. Sci. Eng., B*, 2023, **298**, 116851, DOI: 10.1016/J.MSEB.2023.116851.
3 I. Bourachid, M. Caid and O. Cheref, *et al.*, Insight into the structural, electronic, mechanical and optical properties of inorganic lead bromide perovskite $APbBr_3$ (A = Li, Na, K, Rb,

and Cs), *Comput. Condens. Matter*, 2020, **24**, DOI: 10.1016/j.cocom.2020.e00478.

4 H. Rached, D. Rached and M. Rabah, *et al.*, Full-potential calculation of the structural, elastic, electronic and magnetic properties of $XFeO_3$ (X = Sr and Ba) perovskite, *Phys. B*, 2010, **405**, 3515–3519, DOI: 10.1016/j.physb.2010.05.060.

5 H. Hayashi, H. Inaba and M. Matsuyama, *et al.*, Structural consideration on the ionic conductivity of perovskite-type oxides, *Solid State Ionics*, 1999, **122**, 1–15, DOI: 10.1016/S0167-2738(99)00066-1.

6 H. M. Tütüncü and G. P. Srivastava, Phonons and superconductivity in the cubic perovskite Cr_3RhN, *J. Appl. Phys.*, 2012, 112, DOI: 10.1063/1.4764916/373007.

7 G. Rupprecht and R. O. Bell, Dielectric Constant in Paraelectric Perovskites, *Phys. Rev.*, 1964, **135**, A748, DOI: 10.1103/PhysRev.135.A748.

8 D. Rached, M. Hichour and M. Rabah, *et al.*, Prediction study of the structural, elastic, electronic and optical properties of the antiperovskite $BiNBa_3$, *Solid State Commun.*, 2009, **149**, 2002–2006, DOI: 10.1016/j.ssc.2009.08.033.

9 D. Rached, M. Hichour and M. Rabah, *et al.*, Prediction study of the structural, elastic, electronic and optical properties of the antiperovskite $BiNBa_3$, *Solid State Commun.*, 2009, **149**, 2002–2006, DOI: 10.1016/j.ssc.2009.08.033.

10 H. Benmhidi, H. Rached, D. Rached and M. Benkabou, Ab Initio Study of Electronic Structure, Elastic and Transport Properties of Fluoroperovskite $LiBeF_3$, *J. Electron. Mater.*, 2017, **46**, 2205–2210, DOI: 10.1007/S11664-016-5159-0.

11 J. E. Weidenborner and A. L. Bednowitz, Structures of ferrimagnetic fluorides of ABF_3 type. I. $RbNiF_3$, *Acta Crystallogr., Sect. A*, 1970, **26**, 1464–1468, DOI: 10.1107/S0567740870004338.

12 O. Fukunaga and T. Fujita, The relation between ionic radii and cell volumes in the perovskite compounds, *J. Solid State Chem.*, 1973, **8**, 331–338, DOI: 10.1016/S0022-4596(73)80030-1.

13 K. Ephraim Babu, N. Murali and K. Vijaya Babu, *et al.*, Structural, electronic and elastic properties of $KCaF_3$ and $RbCaF_3$ for vacuum-ultraviolet-transparent lens materials, *AIP Conf. Proc.*, 2015, 1661, DOI: 10.1063/1.4915437/588507.

14 G. Arora, G. Ahuja and U. Ahuja, Electronic and elastic properties of ternary fluoro-perovskite $RbCaF_3$, *J. Phys.: Conf. Ser.*, 2021, **1849**, 012032, DOI: 10.1088/1742-6596/1849/1/012032.

15 J. Saddique, M. Husain and N. Rahman, *et al.*, Modeling structural, elastic, electronic and optical properties of ternary cubic barium based fluoroperovskites $MBaF_3$ (M = Ga and In) compounds based on DFT, *Mater. Sci. Semicond. Process.*, 2022, **139**, 106345, DOI: 10.1016/J.MSSP.2021.106345.

16 B. Bakri, Z. Driss, S. Berri and R. Khenata, First-principles investigation for some physical properties of some fluoroperovskites compounds ABF_3 (A = K, Na; B = Mg, Zn), *Indian J. Phys.*, 2017, **91**, 1513–1523, DOI: 10.1007/S12648-017-1055-6/FIGURES/7.

17 Y. Huang, R. Ding and D. Ying, *et al.*, A F-deficient and high-Mn ternary perovskite fluoride anode with a dominant conversion mechanism for advanced Li-ion batteries, *Chem. Commun.*, 2021, **57**, 7705–7708, DOI: 10.1039/D1CC00910A.

18 M. Husain, N. Rahman and R. Khan, *et al.*, Exploring the exemplary structural, electronic, optical, and elastic nature of inorganic ternary cubic $XBaF_3$ (X = Al and Tl) employing the accurate TB-mBJ approach, *Semicond. Sci. Technol.*, 2022, **37**, 075004, DOI: 10.1088/1361-6641/AC6D00.

19 A. Castro, *Study and Characterization of Magnetic and Multiferroic Materials by First-Principles Calculations*, PhD thesis, Université de Liège, 2016.

20 M. K. Shahzad, S. Hussain and M. Riaz, *et al.*, Investigation of ultra wide bandgap Flouro-perovskite materials $RBeF_3$ (R[dbnd]K and Li) for smart window applications: A DFT study, *Heliyon*, 2024, **10**, 29143, DOI: 10.1016/j.heliyon.2024.e29143.

21 V. Güçkan and Z. Yegingil, *Synthesis of doped fluoroperovskites and oxide ceramics as phosphors and their dosimetric characterization*, Department of physics-Adana, 2021.

22 M. Ali, Z. Bibi and M. W. Younis, *et al.*, An accurate prediction of electronic structure, mechanical stability and optical response of $BaCuF_3$ fluoroperovskite for solar cell application, *Sol. Energy*, 2024, **267**, 112199, DOI: 10.1016/J.SOLENER.2023.112199.

23 M. K. Shahzad, S. Hussain and M. Riaz, *et al.*, Investigation of ultra wide bandgap Flouro-perovskite materials $RBeF_3$ (RK and Li) for smart window applications: A DFT study, *Heliyon*, 2024, **10**, e29143, DOI: 10.1016/J.HELIYON.2024.E29143.

24 M. Springis, L. Brikmane, I. Tale and P. Kulis, *Electronic excitations and defects in fluoroperovskite $LiBaF_3$, 2003, vol. 5122, pp. 23–29, DOI: 10.1117/12.515694.*

25 A. Raja, R. Nagaraj and K. Ramachandran, *et al.*, A facile synthesis, structural and triple-luminescence properties of a novel fluoroperovskite $RbCaF_3:Sm^{3+}$ phosphor for radiation dosimetry and orange-red LED applications, *Mater. Sci. Eng., B*, 2020, **255**, 114531, DOI: 10.1016/J.MSEB.2020.114531.

26 V. Guckan, V. Altunal and G. S. Polymeris, *et al.*, TL and OSL characteristics of the fluoroperovskite $KMgF_3$:Eu,Yb, Li for dosimetry applications, *J. Lumin.*, 2022, **251**, 119213, DOI: 10.1016/J.JLUMIN.2022.119213.

27 F. Hedhili, H. Khan and F. Ullah, *et al.*, Density Functional Theory Unveils the Secrets of $SiAuF_3$ and $SiCuF_3$: Exploring Their Striking Structural, Electronic, Elastic, and Optical Properties, *Molecules*, 2024, **29**(5), 961, DOI: 10.3390/MOLECULES29050961.

28 K. E. Babu, N. Murali, D. T. Swamy and V. Veeraiah, Structural and optoelectronic properties of cubic perovskite $RbPbF_3$, *Bull. Mater. Sci.*, 2014, **37**, 287–293, DOI: 10.1007/S12034-014-0652-7/TABLES/3.

29 Y. Yamane, K. Yamada and K. Inoue, Mechanochemical synthesis and order–disorder phase transition in fluoride ion conductor $RbPbF_3$, *Solid State Ionics*, 2008, **179**, 605–610, DOI: 10.1016/J.SSI.2008.04.022.

30 F. Gulzar, S. Siddique and S. S. A. Gillani, *et al.*, Doping induced modulation in structural, electronic, optical, elastic and mechanical properties of $RbPbF_3$: Insights from DFT computation, *Mater. Sci. Eng., B*, 2024, **305**, 117435, DOI: 10.1016/J.MSEB.2024.117435.

31 I. Ilyas, A. A. Zafar and H. M. Naeem Ullah, *et al.*, Pressure-induced elastic, mechanical and opto-electronic response of

$RbCdF_3$: A comprehensive computational approach, *J. Phys. Chem. Solids*, 2022, **165**, 110642, DOI: 10.1016/J.JPCS.2022.110642.

32 G. Murtaza, Hayatullah and R. Khenata, *et al.*, Elastic and optoelectronic properties of $RbMF_3$ (M = Zn, Cd, Hg): A mBJ density functional calculation, *Phys. B*, 2013, **410**, 131–136, DOI: 10.1016/J.PHYSB.2012.10.024.

33 C. Abderrahmane, L. Brahim and H. Mohamed, *et al.*, First-Principles Study of Structural, Electronic, Optical and Elastic Properties of Cadmium Based Fluoro-Perovskite $MCdF_3$ (M = Rb, Tl), *Solid State Phenom.*, 2019, **297**, 173–186, DOI: 10.4028/WWW.SCIENTIFIC.NET/SSP.297.173.

34 J. A. Abraham, DFT-focused estimation of mechanical, thermoelectric and thermodynamic properties of $ACdF_3$ (A = K, Rb, Cs) fluroperovskites, *Int. J. Mod. Phys. B*, 2019, **33**(27), 1950314, DOI: 10.1142/S0217979219503144.

35 A. Abdullah, S. M. J. Zaidi and M. I. Khan, *et al.*, Assimilation of electronic, elastic, mechanical, optical, and thermal profiles in metal halide perovskite $CsPbCl_3$, for optoelectronic applications, *Comput. Condens. Matter*, 2023, **35**, e00804, DOI: 10.1016/J.COCOM.2023.E00804.

36 M. I. Khan, S. M. J. Zaidi and M. S. U. Sahar, *et al.*, Effect of Stress on Electronic, Optical, Elastic, and Mechanical Properties of Potassium Tantalum Oxide ($KTaO_3$): A DFT Study, *J. Electron. Mater.*, 2023, **52**, 5631–5641, DOI: 10.1007/S11664-023-10484-W/FIGURES/11.

37 M. Riaz, M. S. U. Sahar and S. M. Ali, *et al.*, Investigation of stress-induced effects on structural, optoelectronic, and elastic characteristics of cubic $CaHfO_3$ perovskite oxide; A DFT study, *Comput. Condens. Matter*, 2023, **37**, e00846, DOI: 10.1016/J.COCOM.2023.E00846.

38 S. M. Junaid Zaidi, M. Sana Ullah Sahar and S. Mansoor Ali, *et al.*, Exploring the effects of external stress on the crystal lattice of $SrHfO_3$: Significance of variations in structural, electrical, optical, and mechanical properties, *Results Opt.*, 2023, **13**, 100519, DOI: 10.1016/J.RIO.2023.100519.

39 M. Ijaz Khan, M. Tanveer and M. Sana Ullah Sahar, *et al.*, A comprehensive DFT study on the structural, electronic, elastic, and optical behaviour of $CsPbF_3$ under the effect of stress, *Results Opt.*, 2024, **15**, 100667, DOI: 10.1016/J.RIO.2024.100667.

40 G. Ayub, N. Rahman and M. Husain, *et al.*, Tailoring the structural, elastic, electronic, and optical properties of Cs_2ScCuX_6 (X = Cl and F) double perovskite compounds via density functional theory (DFT), *J. Phys. Chem. Solids*, 2024, 188, DOI: 10.1016/J.JPCS.2024.111942.

41 M. S. U. Sahar, M. I. Khan and S. M. J. Zaidi, *et al.*, Effects of isotropic stress on the band structure elastic, optical, thermal, and X-ray diffraction properties of $TiSnO_3$, *J. Mol. Model.*, 2024, **30**, 247, DOI: 10.1007/S00894-024-06050-8/FIGURES/12.

42 L. Q. Jiang, J. K. Guo and H. B. Liu, *et al.*, Prediction of lattice constant in cubic perovskites, *J. Phys. Chem. Solids*, 2006, **67**, 1531–1536, DOI: 10.1016/J.JPCS.2006.02.004.

43 M. Rousseau, J. Y. Gesland and J. Julliard, *et al.*, Crystallographic, elastic, and Raman scattering investigations of structural phase transitions in $RbCdF_3$ and $TlCdF_3$, *Phys. Rev. B*, 1975, **12**, 1579–1590, DOI: 10.1103/PHYSREVB.12.1579.

44 M. Rizwan, M. Anwar and Z. Usman, *et al.*, Implementation of magnesium doping in $SrTiO_3$ for correlating electronic, structural and optical properties: A DFT study, *Chin. J. Phys.*, 2019, **62**, 388–394, DOI: 10.1016/J.CJPH.2019.09.036.

45 M. Rizwan, Hajra and I. Zeba, *et al.*, Electronic, structural and optical properties of $BaTiO_3$ doped with lanthanum (La): Insight from DFT calculation, *Optik*, 2020, **211**, 164611, DOI: 10.1016/J.IJLEO.2020.164611.

46 M. Shakil, M. Kousar and S. S. A. Gillani, *et al.*, First principle computation of half metallicity and mechanical properties of a new series of half Heusler alloys KMnZ (Z = B, Si, Ge, As) for spintronics, *Indian J. Phys.*, 2022, **96**, 115–126, DOI: 10.1007/S12648-020-01967-1/TABLES/7.

47 M. Shakil, A. Akram and I. Zeba, *et al.*, Effect of mixed halide contents on structural, electronic, optical and elastic properties of $CsSnI_{3-x}Br_x$ for solar cell applications: first-principles study, *Mater. Res. Express*, 2020, **7**, 025513, DOI: 10.1088/2053-1591/AB727D.

48 J. Chen, X. Zhang, L. Yang and F. Wang, The vacancy defects and oxygen atoms occupation effects on mechanical and electronic properties of Mo_5Si_3 silicides, *Commun. Theor. Phys.*, 2021, **73**, 045702, DOI: 10.1088/1572-9494/ABE367.

49 J. Chen, X. Zhang, L. Yang and F. Wang, The vacancy defects and oxygen atoms occupation effects on mechanical and electronic properties of Mo_5Si_3 silicides, *Commun. Theor. Phys.*, 2021, **73**, 045702, DOI: 10.1088/1572-9494/ABE367.

50 F. Hofer, F. P. Schmidt, W. Grogger and G. Kothleitner, Fundamentals of electron energy-loss spectroscopy, *IOP Conf. Ser.: Mater. Sci. Eng.*, 2016, **109**, 012007, DOI: 10.1088/1757-899X/109/1/012007.